Robust strong coupling architecture in circuit quantum electrodynamics

Rishabh Upadhyay[1], George Thomas [1], Yu-Cheng Chang[1], Dmitry S. Golubev[1], Andrew Guthrie[1], Azat Gubaydullin[1], Joonas T. Peltonen[1], and Jukka P. Pekola[1]
Pico group, QTF Centre of Excellence, Department of Applied Physics, Aalto University School of Science, P.O. Box 13500, 00076 Aalto, Finland

We report on a robust method to achieve strong coupling between a superconducting flux qubit and a high-quality quarter-wavelength coplanar waveguide resonator. We demonstrate the progression from the strong to ultrastrong coupling regime by varying the length of a shared inductive coupling element, ultimately achieving a qubit-resonator coupling strength of 655 MHz, 10% of the resonator frequency. We derive an analytical expression for the coupling strength in terms of circuit parameters and also discuss the maximum achievable coupling within this framework. We experimentally characterize flux qubits coupled to superconducting resonators using one and two-tone spectroscopy methods, demonstrating excellent agreement with the proposed theoretical model.

arXiv:2107.11135v1 [quant-ph] 23 Jul 2021

I. INTRODUCTION

Research over the past few decades has seen significant progress in the field of superconducting quantum circuits[1,2], making such systems the dominant platform for the realization of novel quantum devices. The framework, incorporating superconducting qubits[3–6] and cavity resonators, is known by the name circuit quantum electrodynamics (c-QED): the superconducting circuit variant of 'cavity QED'. Superconducting qubits as two-level systems, also known as 'artificial atoms', are the most researched and robust candidates for various applications in the field of c-QED. The advancement in realizing controllable interaction between these artificial atoms and cavities has developed enormously in recent years. Employing a multitude of quantum device architectures, the realization of various qubit-cavity coupling regimes has been explored. The atom-cavity strong coupling regime[7–9] and ultrastrong coupling regime[10–15], where an artificial atom and the cavity exchange a photon many times before the coherence vanishes, has emerged and has been studied extensively.

In this work, we experimentally demonstrate a simple, systematic and robust architecture to achieve strong qubit-resonator coupling. To realize this, we exploit the geometric inductance and nonlinear kinetic inductance of the coupling element by increasing its length and/or decreasing the cross sectional area. The concept of a shared local inductance as a coupling element has been previously explored both theoretically[16] and experimentally[7]. A related approach takes advantage of a large nonlinear inductance by embedding a fourth Josephson junction, also known as a 'coupling junction'[12,16]. However, the Josephson energy E_J, a crucial parameter in flux qubits, is exponentially sensitive to the tunnel barrier thickness[6,17], determined mainly by the junction dimensions and oxidation parameters. From fabrication point of view, adding an extra junction adds complexities in the functionality of a flux qubit by influencing the qubit energy levels. Furthermore, optimizing and controlling the coupling junction parameters can be a cumbersome process and challenging in terms of reproducibility and yield. Nevertheless, the architecture of a coupling junction at the constricted central line of a coplanar waveguide (CPW) is a practical choice to achieve ultra strong coupling, while isolating the qubit from magnetic flux noise. References[18,19]report on the dependence of magnetic flux noise magnitude over the superconducting loop area. Furthermore, local effects in the superconducting material and substrate can produce magnetic flux noise[20–23]. In our devices we use a wide array of flux trapping holes to insulate the flux qubits from magnetic flux noise[23–27].

In this paper, we demonstrate the linear dependence of qubit-resonator coupling g while increasing the length dependent inductance of a shared coupling element. Using this robust coupling architecture we show how ultrastrong coupling can be achieved without the use of a coupling junction. Our framework is useful for quantum thermodynamic experiments since the heat current is proportional to the square of the coupling between a qubit and the resonator employed for spectral filtering[28,29].

II. DEVICE AND MEASUREMENTS

We report on the fabrication and measurement of seven qubit-resonator systems with varying coupling strengths. As shown in Fig. 1(a), the measured device houses seven $\lambda/4$ resonators of varying frequency, capacitively coupled to a common feedline, as shown in Fig. 1(b). The end of each resonator is shunted to a common ground, facilitating inductive coupling to a flux qubit by sharing an inductive element between qubit and the resonator, here labelled a *'shared edge'*, as shown in Fig. 1(d). Depending upon the geometry of this shared edge, the strength of the coupling between qubit and the resonator can vary. Ultra strong coupling is achieved by fabricating the long meandering shared edge structure as shown in Fig. 1(d). Our frequency multiplexing scheme allows us to study multiple flux qubits simultaneously, providing a common platform for comparison. The studied devices are embedded on a 675 μm thick, highly resistive Si wafer. Ground

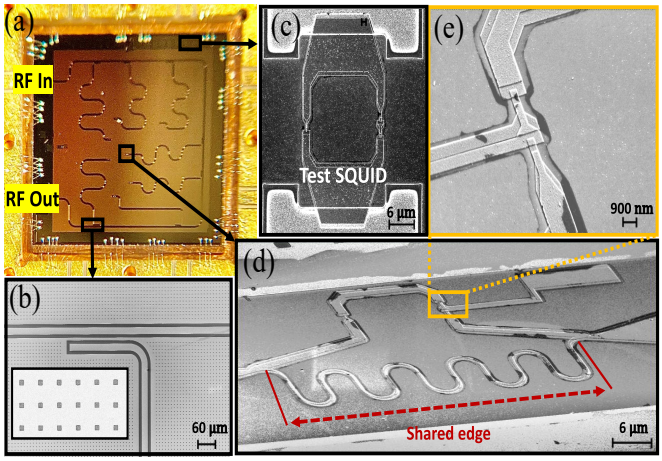

FIG. 1. The studied structure (a). Microscopic view of the reported device. (b). Electron micrograph showing the capacitive coupling of a diagnostic resonator to a common feedline and an enlarged array of flux trapping holes in the inset. (c). Electron micrograph of the test SQUID. (d). 3 junction flux qubit with 120 μm long meander element producing the large coupling. (e). Electron micrograph of two large identical junctions of a flux qubit.

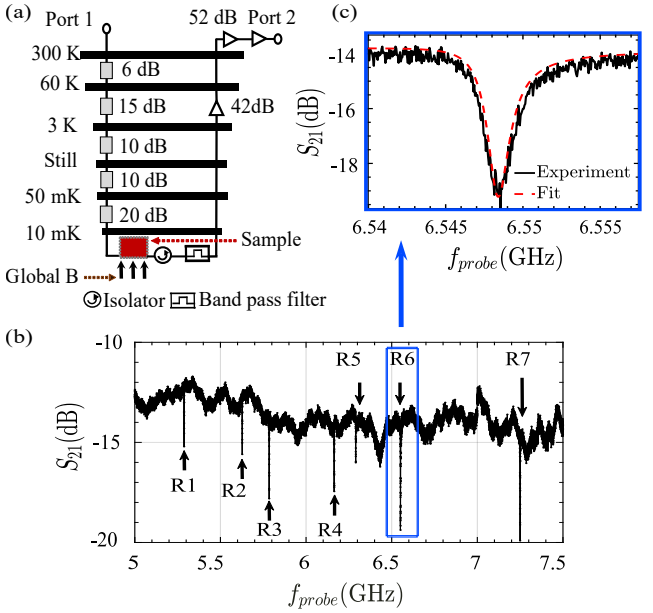

FIG. 2. (a). Employed measurement setup scheme. (b). Broad range S_{21} transmission confirming the presence of seven superconducting resonators indicated by vertical arrows. (c). Fitted notch type transmission of one of the superconducting resonators based on the transmission S_{21} vs. frequency. The red dashed line shows a fit to the experimental data using Eq. (1)

planes and resonators are formed by etching a 200 nm thick DC sputtered superconducting niobium. Using the Dolan bridge technique, two 30 nm thick layers of aluminium metal are evaporated at design-specific tilt angles interrupted by an in-situ oxidation to form the oxide barrier[30]. The fabrication details are broadly reported in Appendix A. The reliability of fabrication was verified by measuring room temperature resistance of test junctions present in the same fabrication batch. The room temperature resistance of the identical three junction test SQUID Fig. 1(c) is $R \approx 5$ kΩ. The sample is diced using a saw with a thin diamond-embedded resin blade. The device is wire-bonded to a printed circuit board and mounted to the mixing chamber of a commercial dilution refrigerator with a base temperature of 10 mK.

To identify the superconducting resonators, the transmission S_{21} is measured in a broad frequency range by applying a microwave signal from a vector network analyzer (VNA) located at room temperature. Black-body radiation is suppressed using of a series of impedance matched cryogenic attenuators distributed at various temperature stages within the cryostat. The output signal passes through two isolators positioned at the cryostat base temperature, and further amplified by a 42 dB low noise HEMT amplifier mounted at the 4 K stage. Outside the cryostat, the signal is further amplified by 52 dB using two additional room temperature amplifiers. The employed measurement scheme is displayed in Fig. 2(a). Figure 2(b) shows the measured transmission S_{21} from 5.0 GHz to 7.5 GHz showing the presence of seven peaks, corresponding to seven superconducting resonators of varying frequency. Furthermore, Fig. 2 (c) presents a fitted S_{21} transmission corresponding to the qubit with highest measured coupling. The S_{21} scattering parameter expression used to fit the notch-type profile of fabricated superconducting resonators reads[31–34]

$$S_{21}^{\text{notch}} = ae^{i\alpha}e^{-2\pi i f\tau}\left[1 - \frac{(Q_l/|Q_c|)e^{i\phi}}{1 + 2iQ_l(f/f_r - 1)}\right]. \quad (1)$$

In this expression, a corresponds to the overall signal amplitude, phase shift due to various circuit components is given by α and electronic delays by τ[31–34]. In the ideal resonator part f, f_r, Q_l and $|Q_c|$ denote the probe frequency, bare resonator frequency, loaded quality factor and the coupling (or external) quality factor in absolute terms, respectively. In Eq. 1, $e^{i\phi}$ signifies the on-chip impedance mismatch, caused by the standing waves and signal asymmetries from different ports[8,33]. In a resonator f_r and Q are two important characteristics, f_r is length dependent and $|Q_c|$ is determined by the coupling architecture of the resonator to a transmission line[35]. By fitting the S_{21} we determine the internal quality factor $Q_i \approx 5200$, loaded quality factor $Q_l \approx 2800$ and coupling quality factor $Q_c \approx 6000$ of our superconducting resonator. In a resonator Q_i and $|Q_c|$ are the two prominent energy relaxations paths[33]. The total quality factor Q_l of a resonator is given by[31,36]

$$Q_l^{-1} = Q_i^{-1} + \text{Re}\{Q_c^{-1}\}. \quad (2)$$

The depth of the notch type transmission profile is defined by the ratio of Q_l and Q_c, maximizing at the resonator frequency where $Q_l \approx Q_c$. The photon decay rate $\kappa/2\pi(=\omega/Q_l)$, calculated based on the value of Q_l from fitting Fig. 2 (c) is 0.37 MHz, corresponding to the photon lifetime $T_r = 1/\kappa$ of 427 ns. For fast spectroscopy measurements to probe the states of a qubit, resonators with moderate quality factor (strongly coupled) are an ideal choice[8,35]. We then measure the dispersive shift dependence of the diagnostic resonators, as a function of applied flux bias. This is done by measuring the S_{21} transmission through the common feed line while sweeping the magnet coil current. Due to the coupling between the individual resonators and qubits, the shift from bare resonator frequency is detected while varying the magnet coil current determining the Josephson energy. Furthermore, to locate the individual qubit transitions we perform two-tone spectroscopy. Here, a weak microwave 'probe tone' (tone 1), supplied using a VNA, is continuously applied via the readout resonator at a specific magnet coil bias voltage. Once the flux specific probe frequency is located, a 'pump tone' (tone two) is applied using a separate microwave signal generator to excite the qubit energy levels. To estimate the coupling strengths, the measured dispersive shift and explored qubit states are fitted using our theoretical model.

III. THEORETICAL MODEL

Here we consider a conventional flux qubit which is composed of a superconducting ring interrupted by three Josephson junctions as shown in Fig. 3[4,5]. The junctions numbered 1 and 2 are nominally identical with equal critical currents $I_{C1} = I_{C2} = I_C$ and the critical current of the third junction is $I_{C3} = \alpha I_C$, where the factor (ratio between the area of junction 3 and 1) $\alpha < 1$. There are two superconducting islands in this setup, the first island (G_1) is limited by junctions 1 and 2 and the capacitor C_{g1} with total capacitance of the island $C_{G1} = C_1 + C_2 + C_{g1}$. The second island ($G_2$) is sandwiched by junctions 2 and 3 and the capacitor C_{g2}, with a total capacitance $C_{G2} = C_2 + C_3 + C_{g2}$. The element between the junction 1 and 3 is shared by both the qubit and the resonator and the inductance of this element is responsible for the qubit-resonator coupling. The phase drop across the shared edge (due to inductance) is $\varphi = \varphi_1 + \varphi_2 + \varphi_3 - 2\pi\varphi_{\rm ext}$, where φ_i is the phase drop across the ith junction and $\varphi_{\rm ext} = 2\pi\Phi_{\rm ext}/\Phi_0$, while the external magnetic flux is $\Phi_{\rm ext}$ and $\Phi_0 = h/2e$ is the magnetic flux quantum. The total Hamiltonian of the system is given as $H = H_{\rm res} + H_{\rm loop} + H_{\rm int}$, where that of the resonator in terms of the ladder operators (a_n, $a_n^\dagger$) and frequency of the nth mode ω_n is $H_{\rm res} = \sum_{n=0}^{\infty} \hbar\omega_n \left(a_n^\dagger a_n + \frac{1}{2}\right)$.

The Hamiltonian of the loop consisting of the qubit

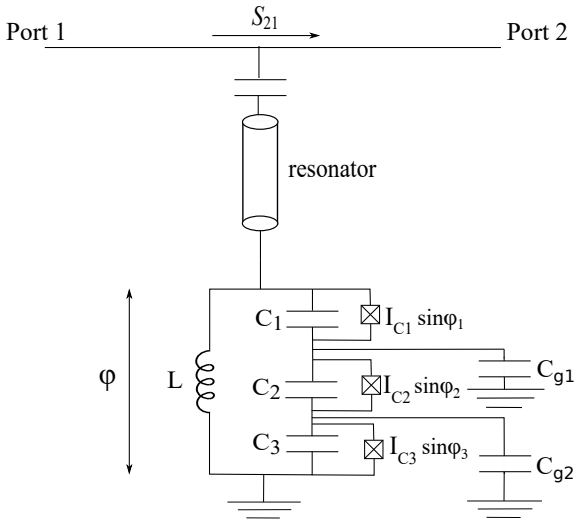

FIG. 3. Circuit diagram of a three junction flux qubit coupled to a resonator. The resonator is capacitively coupled to a transmission line with which a S_{12} measurement is carried out. There are seven similar qubit-resonator systems coupled to a single transmission line (1-2) as shown in Fig. 1(a).

and the shared edge is

$$H_{\rm loop} = \sum_{r,s=1}^{3} 4(E_C)_{rs} n_r n_s + \sum_{j=1}^{3} \frac{\hbar I_{Cj}}{2e}(1-\cos\varphi_j) + \frac{\hbar^2\varphi^2}{8e^2 L}, \tag{3}$$

where L is the inductance of the shared edge. Here $n_r = -i\partial/\partial\varphi_r$, $(E_C)_{rs} = e^2(C^{-1})_{rs}/2$ and the capacitance matrix is

$$C = \begin{bmatrix} C_1 & 0 & 0 \\ 0 & C_{g1}+C_2 & C_{g1} \\ 0 & C_{g1} & C_{g1}+C_{g2}+C_3 \end{bmatrix}. \tag{4}$$

The qubit-resonator interaction Hamiltonian is

$$H_{\rm int} = -\sum_{n=0}^{\infty} \hbar\sqrt{\frac{R_q\omega_0\omega_n}{4\pi^2 Z_0}}\,\varphi(a_n^\dagger + a_n) + \sum_{n=0}^{\infty} \frac{R_q}{4\pi^2 Z_0}\hbar\omega_0\varphi^2, \tag{5}$$

where $R_q = h/e^2$ is the resistance quantum and ω_0 is the fundamental frequency of the resonator. Equation (5) is a general case where the summation shows that the phase φ couples to all modes of the resonator. When the bare qubit frequency ω_q is close to ω_0, for low cryostat temperatures and low power S_{21} measurements, we can ignore the contributions from higher modes of the resonators and take $n = 0$. In our model, the qubit is inductively coupled to the resonator via the shared element and the inductance of the shared edge has two contributions, $L = L_{\rm geo} + L_{kin}$, where $L_{\rm geo}$ is the geometric inductance and $L_{kin} = \hbar R_n/\pi\Delta$ is the kinetic inductance of the the aluminum wire, whose resistance

in normal state is R_n and superconducting gap of aluminum wire $\Delta = 200$ μeV. The resistivity of the shared edge is estimated in our case to be $5.3 \times 10^{-8}\,\Omega\,\mathrm{m}$, measured at room temperature across an evaporated Al strip of area ≈ 4900 $\mu\mathrm{m}^2$, embedded in the reported device. We explicitly derive (see Appendix B) the coupling in terms of circuit parameters as

$$g \approx \beta \frac{L_J^{-1}}{L^{-1} + L_J^{-1} + L_r^{-1}} \sqrt{\frac{1-\alpha}{L_r C_{\mathrm{eff}}}}. \tag{6}$$

where $L_J = L_1 = L_2 = \hbar/2eI_{C1}$ and $L_r = \pi Z_0/4\omega_0$ is the total inductance of the resonator and the effective capacitance of the qubit is given by

$$C_{\mathrm{eff}} = \big[(C_{G1}(1-\alpha) - 2C_2)^2 + 4(C_{G2} - C_2)^2 + 4\alpha(C_{G1}C_{G2} - 2C_2^2) \big]^{1/2}. \tag{7}$$

Equation (6) is derived for a linearized model, where we replace Josephson junctions with inductors and we get $\beta = 1/2$. This approximation may not be valid close to the flux value $\Phi/\Phi_0 = 0.5$. By fitting with the experimental data, we get $\beta = 1/4$ as shown in Fig. 5. Equation (6) is useful for efficient circuit design as the coupling is expressed in terms of circuit parameters.

IV. RESULTS AND DISCUSSION

It is evident from Eq. (6) that we can increase the coupling by increasing the inductance which in turn can be achieved by increasing the length, or decreasing the thickness of the shared element. The width of the shared edge $w \approx 0.44$ μm for the qubits numbered 1, 2, 4, 5, and 6 and length of the shared edge of each of these qubits are different and varies from $l = 10$ μm to $l = 120$ μm, while $w \approx 0.35$ μm for the qubits 3 and 7, as shown in Fig. 1(a) and in Table I. We have two sets of qubits with equal length and different widths: the length $l = 30$ μm for the qubits 2 and 3, and $l = 120$ μm for qubits 6 and 7. In this way inductance of the shared edge varies for all qubits. The thickness of shared edge is approximately 60 nm for all the qubits.

We perform both one-tone and two-tone spectroscopy to characterize the resonators and qubits. By fitting the one-tone spectra, we get the coupling between the qubit and the resonator, and the two-tone spectra provides the qubit transition frequencies. To find the coupling g between qubit and the resonator, in the experiment, we fit the experimental data in the following way. First we find ω_q by diagonalizing the qubit Hamiltonian in Eq. (3) setting $L = 0$. We use two-dimensional plane waves $\exp(-in_1\varphi_1 - in_3\varphi_3)/(2\pi)$ to numerically diagonalize the Hamiltonian (Eq. (3)) to find ω_q. The dressed frequencies of qubit and resonator are given

$$\omega'_{q/r} = \frac{1}{\sqrt{2}} \sqrt{\omega_q^2 + \omega_r^2 \pm \sqrt{16g^2\omega_q\omega_r + (\omega_q^2 - \omega_r^2)^2}}. \tag{8}$$

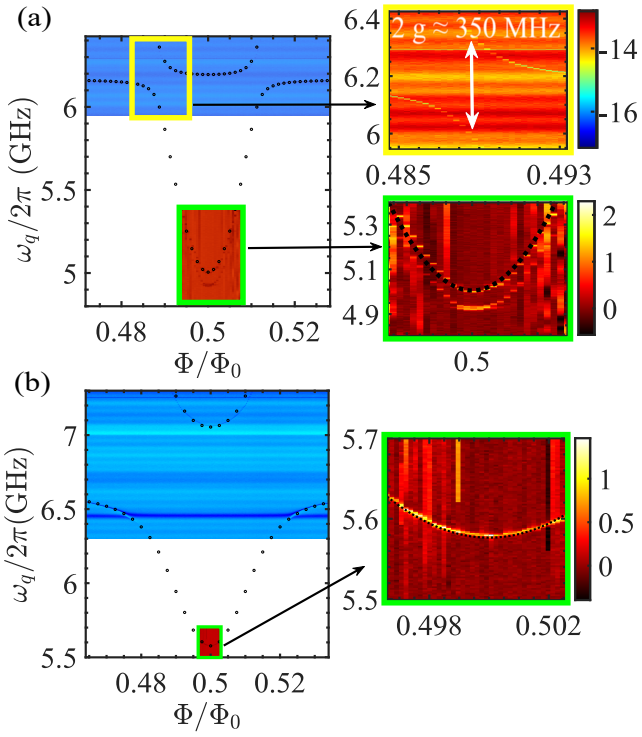

FIG. 4. One-tone and two-tone spectroscopy of the qubits for (a) shared coupling element length $l = 0.30$ μm with $g/2\pi = 180$ MHz (b) shared coupling element length 120 μm and $g/2\pi = 655$ MHz. The width of both coupling elements is 0.35 μm. In (a) and (b), the upper part of the figure in the left side shows a limited segment of the one-tone spectra where the $2g$ value is estimated based on experimental observation while figure in the bottom (framed in yellow and enlarged on the right-side) represents two-tone spectra. The dotted lines show the theoretical model using Eq. (8). In (a), the experimental data in the green box are enlarged on the right side. In (a) we have $E_J/h = 68.75$ GHz, $\alpha = 0.5825$, $\omega_r/2\pi = 6.170$ GHz and in (b) $E_J/h = 65.2$ GHz, $\alpha = 0.547$, $\omega_r/2\pi = 6.685$ GHz.

Using Eq. (8), we fit the data obtained from one-tone and two-tone spectroscopy simultaneously. As an example, spectroscopy of the two qubits, 3 and 7, with shared edge lengths 30 μm and 120 μm are shown in Fig. 4. The fitted one-tone and two-tone spectra of qubits numbered 1, 2, 4, 5 and 6 are shown in Appendix A. Furthermore, we compare the coupling obtained from the experiments with the estimated coupling from Eq. (6). For qubits numbered 1, 2, 3, 4, 5, and 7, the error in the coupling estimation is typically ± 5 %, while the error for qubit 6 is -12 %, $+8$ %. For each qubit, the error is estimated by varying the coupling term (g) within a reasonable

No.	l μm	w μm	$\omega_r/2\pi$ GHz	L nH	$(g/\omega_r)100$ %
1	10	0.44	5.629	0.031	1.40
2	30	0.44	5.291	0.095	2.74
3	30	0.35	6.170	0.130	2.91
4	60	0.44	5.798	0.191	4.19
5	90	0.44	7.277	0.285	6.39
6	120	0.44	6.330	0.365	9.32
7	120	0.35	6.685	0.587	9.80

TABLE I. Parameters of the seven qubit-resonator systems shown in Fig. 1(a).

range, while keeping other fitting parameters unchanged. As illustrated in Fig. 5, the coupling increases linearly with the total inductance of the shared edge. It can be seen from Eq. (6) that by increasing the critical current of the junction (thereby decreasing L_J) coupling can be increased. It also shows that for $L \gg \min\{L_r, L_J\}$, the coupling saturates to its maximum value. For $\alpha = 1/2$, $g/\omega_r = L_r/(4[L_r + L_J])\sqrt{C_r/(C_{G1} + 4C_{G2} - 4C_2)}$, with parameters considered in this manuscript, we could achieve a maximum coupling of 25% of resonator frequency.

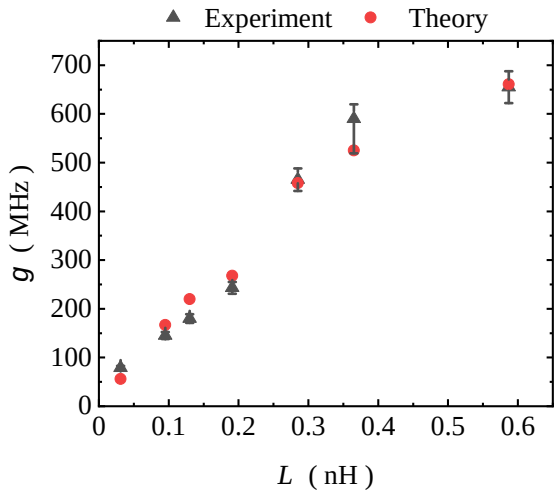

FIG. 5. Measured coupling for the seven qubits together with the prediction from the theoretical model given in Eq. (6) with $\beta = 1/4$. The qubits 3 and 7 are shown in Fig. 4.

Conclusion: In conclusion, we demonstrate experimentally a simple and robust approach towards achieving high coupling strength between a qubit and resonator by exploiting the length dependent inductance of a galvanic coupling element. We introduce a theoretical model which supports the experimental results, deriving an expression for g in terms of circuit parameters which is useful for highly efficient design of quantum circuits. Our model with strong coupling between flux type qubits and resonators can play a major role, e.g. in heat transport devices[28,29,37].

Acknowledgment: This work was financially supported through Academy of Finland grants 297240, 312057 and 303677 and from the European Union's Horizon 2020 research and innovation programme under the European Research Council (ERC) programme (grant number 742559) and Marie Sklodowska-Curie actions (grant agreements 766025). We also thank the Russian Science Foundation (Grant No. 20-62-46026) for supporting the work. We sincerely acknowledged the provision of facilities by Micronova Nanofabrication Centre and OtaNano - Low Temperature Laboratory of Aalto University to perform this research and VTT Technical Research Center for sputtered Nb films.

Appendix A: Fabrication and measurements

The devices are fabricated on a 675 μm thick, highly resistive Si wafer. A 30 nm thick Al_2O_3 is deposited using atomic layer deposition (ALD), followed by DC magnetron sputtering of a 200 nm superconducting niobium (Nb) layer. For patterning the common feedline, ground plane and resonators, a 300 nm thick positive electron beam resist layer is spin-coated onto the substrate. Nb patterns are exposed by Electron Beam Lithography. After development the sample is post-baked for 5 minutes at 150 °C, followed by reactive ion etching of the exposed parts using CF_4 + O_2 chemistry. Post-baking is done to improve resist adhesion. To create the Aluminium layers and Josephson junctions we use the standard Dolan Bridge technique using a bilayer PMMA/MMA resist. After exposure, the top resist layer is developed in Methyl-Isobutyl-Ketone (MIBK):Isopropanol alcohol (IPA) developer solution, and the bottom layer is developed in Methyl-glycol:Methanol solution. Deposition is performed using an e-beam evaporator. In-situ argon plasma milling is used to etch any native oxide formed on the sample surface. A 30 nm thick layer of aluminium metal is evaporated at +18° followed by oxidation to form the barrier oxide. Subsequently, a second 30 nm thick aluminium layer is evaporated at −18°. The evaporated metal from the unexposed part is then lifted-off using acetone. The sample is finally diced and prepared for spectroscopy measurements.

In Fig. 6, we present fitted one tone and two tone spectra of qubits numbered 1, 2, 4, 5, and 6 with their respec-

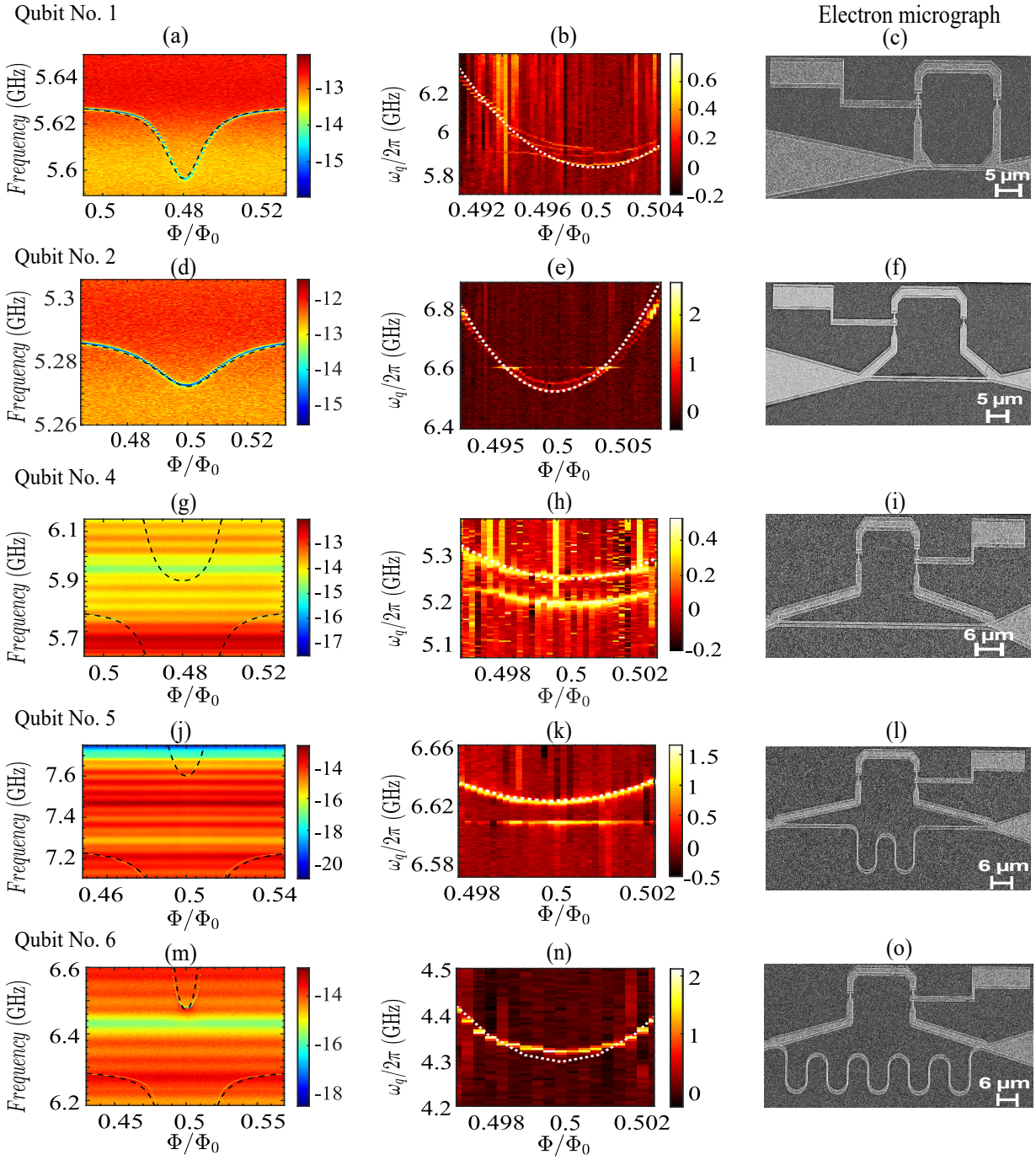

FIG. 6. In each row the figures from left to right represent one tone spectra, two-tone spectra and electron micrograph of qubits reported in Table I.

tive electron micrograph on the third column. Parameters used for fitting are broadly reported in Table II, for qubit numbered 1, 2, 4, 5, and 7, $C_1 = 8.68$ fF, $C_2 = 8.18$ fF, $C_{g1} = 3.65$ fF and $C_{g2} = 3.70$ fF while for qubit numbered 6, we get $C_1 = 7.95$ fF, $C_2 = 8.15$ fF, $C_{g1} = 3.60$ fF and $C_{g2} = 3.57$ fF.

Appendix B: Theory

Derivation of Eq. (6) in the main text:

We consider the system depicted in Fig. 4 of the main text. To derive an appoximate expression for the coupling strength g, we linearize the dynamics of the Josephson junctions and approximately replace them by induc-

No.	C_3 fF	E_J GHz	α	$g/2\pi$ MHz experiment	$g/2\pi$ MHz theory
1	4.73	64.8	0.5542	79	56
2	4.57	67.20	0.5325	145	167
3	4.93	68.75	0.5825	180	220
4	4.81	60.5	0.565	243	268
5	4.45	66	0.5157	465	460
6	5.25	77	0.595	590	525
7	4.67	65.2	0.547	655	661

TABLE II. Parameters of the seven qubit-resonator systems shown in Fig. 1(a).

tors $L_j(\Phi)$, which depend on the magnetic flux Φ and are given by

$$\frac{1}{L_1(\Phi)} = \frac{2eI_{C1}}{\hbar}\cos\left(\varphi_2^{\rm eq}+\varphi_3^{\rm eq}-2\pi\frac{\Phi}{\Phi_0}\right),$$
$$\frac{1}{L_2(\Phi)} = \frac{2eI_{C2}}{\hbar}\cos\varphi_2^{\rm eq},$$
$$\frac{1}{L_3(\Phi)} = \frac{2eI_{C3}}{\hbar}\cos\varphi_3^{\rm eq}. \quad \text{(B1)}$$

Here $\varphi_j^{\rm eq}$ are the flux dependent equilibrium values of the Josephson phases, which are determined by the current balance conditions

$$I_{C1}\sin\left(\varphi_2^{\rm eq}+\varphi_3^{\rm eq}-2\pi\frac{\Phi}{\Phi_0}\right)+I_{C2}\sin\varphi_2^{\rm eq}=0,$$
$$I_{C1}\sin\left(\varphi_2^{\rm eq}+\varphi_3^{\rm eq}-2\pi\frac{\Phi}{\Phi_0}\right)+I_{C3}\sin\varphi_3^{\rm eq}=0. \quad \text{(B2)}$$

Defining small deviations of the phases from their equilibrium values, $\phi_j=\varphi_j-\varphi_j^{\rm eq}$, and expanding the nonlinear terms in the Hamiltonian (3) to the order $\propto\phi_j^2$, we obtain the harmonic approximation for the Hamiltonian of the isolated qubit,

$$H_{\rm loop}^{\rm harm} = -\frac{2e^2}{C_{G1}C_{G2}-C_2^2}\left[(C_{G1}+C_{G2}-2C_2)\frac{\partial^2}{\partial\phi_2^2}+C_{G1}\frac{\partial^2}{\partial\phi_3^2}-2(C_{G1}-C_2)\frac{\partial^2}{\partial\phi_2\partial\phi_3}\right]+\frac{(\phi_2+\phi_3)^2}{2L_1(\Phi)}+\frac{\phi_2^2}{2L_2(\Phi)}+\frac{\phi_3^2}{2L_3(\Phi)}. \quad \text{(B3)}$$

The classical Lagrangian of the qubit in this approximation takes the form

$$\mathcal{L}_{\rm loop}^{\rm harm} = \frac{C_2}{2}\left(\frac{\hbar\dot\phi_2}{2e}\right)^2+\frac{C_3+C_{g2}}{2}\left(\frac{\hbar\dot\phi_3}{2e}\right)^2+\frac{C_1+C_{g1}}{2}\left(\frac{\hbar\dot\phi_2}{2e}+\frac{\hbar\dot\phi_3}{2e}\right)^2-\frac{\hbar^2(\phi_2+\phi_3)^2}{8e^2L_1(\Phi)}-\frac{\hbar^2\phi_2^2}{8e^2L_2(\Phi)}-\frac{\hbar^2\phi_3^2}{8e^2L_3(\Phi)} \quad \text{(B4)}$$

Solving the corresponding classical equations of motion for the phases ϕ_j, we find the two eigen-frequencies of the qubit,

$$\omega_{q_1,q_2}^2 = \frac{\frac{C_{G1}}{L_2}+\frac{C_{G1}}{L_3}+\frac{C_{G2}}{L_2}+\frac{C_{G2}}{L_1}-\frac{2C_2}{L_2}}{2(C_{G1}C_{G2}-C_2^2)} \pm \frac{1}{2(C_{G1}C_{G2}-C_2^2)}\left[\left(\frac{C_{G1}}{L_2}+\frac{C_{G1}}{L_3}+\frac{C_{G2}}{L_2}+\frac{C_{G2}}{L_1}-\frac{2C_2}{L_2}\right)^2 -4(C_{G1}C_{G2}-C_2^2)\left(\frac{1}{L_1L_2}+\frac{1}{L_1L_3}+\frac{1}{L_2L_3}\right)\right]^{1/2}. \quad \text{(B5)}$$

For the parameters of our qubits the frequency ω_{q_1} turns out to be very high. In contrast, the frequency ω_{q_2} is lower and it approaches the resonator frequency ω_r at flux values close to $\Phi_0/2$.

We now include the interaction with the resonator into the model and leave only its fundamental mode with the frequency ω_r. Afterwars, the Lagrangian of the system takes the form

$$\mathcal{L} = \frac{\hbar^2}{8e^2}\Big\{C_1\dot\phi^2-\frac{\phi^2}{L}+C_{G1}\dot\phi_2^2+(C_{G1}+C_{G2}-2C_2)\dot\phi_3^2 +2(C_{G1}-C_2)\dot\phi_2\dot\phi_3-\frac{(\phi-\phi_2-\phi_3)^2}{L_1}-\frac{\phi_2^2}{L_2}-\frac{\phi_3^2}{L_3} -2C_1(\dot\phi_2+\dot\phi_3)\dot\phi+\frac{4}{\pi Z_0\omega_r}\left[\dot\phi_n^2-\omega_n^2(\phi_n-\phi)^2\right]\Big\} \quad \text{(B6)}$$

Here we defined the phase

$$\phi=\varphi_1+\varphi_2+\varphi_3-(\varphi_1^{\rm eq}+\varphi_2^{\rm eq}+\varphi_3^{\rm eq}). \quad \text{(B7)}$$

The Lagrangian (B6) describes four coupled oscillators. We define the vector of phases $\boldsymbol{\phi}^T=(\phi,\phi_3,\phi_2,\phi_n)$ and the matrices

$$M=\begin{pmatrix} C_1 & -C_1 & -C_1 & 0\\ -C_1 & C_{G1}+C_{G2}-2C_2 & C_{G1}-C_2 & 0\\ -C_1 & C_{G1}-C_2 & C_{G1} & 0\\ 0 & 0 & 0 & C_r\end{pmatrix},$$
$$V=\begin{pmatrix} \frac{1}{L}+\frac{1}{L_1}+C_r\omega_n^2 & -\frac{1}{L_1} & -\frac{1}{L_1} & -C_r\omega_n^2\\ -\frac{1}{L_1} & \frac{1}{L_3}+\frac{1}{L_1} & \frac{1}{L_1} & 0\\ -\frac{1}{L_1} & \frac{1}{L_1} & \frac{1}{L_2}+\frac{1}{L_1} & 0\\ -C_r\omega_n^2 & 0 & 0 & C_r\omega_n^2\end{pmatrix}.$$

Here $C_r=4/\pi Z_0\omega_r$ is the effective capacitance of the resonator. The eigen-frequencies of the system are determined by the equation

$$\det\left[M\omega^2-V\right]=0, \quad \text{(B8)}$$

which has four solutions. Two of these solutions correspond to the anti-crossing between the resonator mode ω_r and the low frequency qubit mode $\omega_{q_2}(\Phi)$. This anti-crossing can be approximately described by the model of

two coupled oscillators (see also Eq. (7) in the main text)

$$\omega' \approx \sqrt{\frac{\omega_{q_2}^2 + \omega_r^2 \pm \sqrt{(\omega_{q_2}^2 - \omega_r^2)^2 + 16 g^2 \omega_{q_2} \omega_r}}{2}}. \quad \text{(B9)}$$

In our sample the junctions 1 and 2 have the same inductance $L_J = L_1 = L_2 = \hbar/2eI_{C1}$, while the junction 3 with the weaker critical current has larger inductance $L_3 = L_J/\alpha$. In addition to that, the condition $\omega_r \ll \omega_p$, where $\omega_p = 1/\sqrt{L_J C_1}$ is the plasma frequency of the junctions 1 and 2, is fulfilled. Under these conditions, the qubit frequency $\omega_{q_2}(\Phi)$ approaches the resonator frequency ω_r at $\Phi \approx \Phi_0/2$. At this flux point one can approximately solve Eqs. (B2) for the junction phases and, afterwards, Eq. (B8) for the frequencies. Comparing the result with Eq. (B9), we obtain the approximate expression for the coupling constant g in the form of Eq. (6) with $\beta = 1/2$.

[1] G. Wendin and V. S. Shumeiko, Superconducting quantum bits, arXiv:cond-mat/0508729 (2005).

[2] X. Gu, A. F. Kockum, A. Miranowicz, Y. Liu and F. Nori, Physics Reports **718**, 1 (2017).

[3] J. Clarke and F. K. Wilhelm, Superconducting quantum bits, Nature **453**, 1031 (2008).

[4] T. P. Orlando, J. E. Mooij, L. Tian, C. H. van der Wal, L. S. Levitov, S. Lloyd, and J. J. Mazo, A Superconducting persistent-current qubit, Phys. Rev. B **60**, 15398 (1999).

[5] J. E. Mooij, L. Tian, C. H. van der Wal, L. S. Levitov, S. Lloyd, and J. J. Mazo, Josephson Persistent-Current Qubit, Science **285**, 1036 (1999).

[6] M. H. Devoret, A. Wallraff and J. M. Martinis, Superconducting Qubits: A Short Review, arXiv:cond-mat/0411174 (2004).

[7] A. A. Abdumalikov, O. Astafiev, Y. Nakamura, Yu. A. Pashkin and J. Tsai, Vacuum Rabi splitting due to strong coupling of a flux qubit and a coplanar-waveguide resonator, Phys. Rev. B **78**, 180502(R) (2008).

[8] A. Wallraff, D. I. Schuster, A. Blais, L. Frunzio, R. S. Huang, J. Majer, S. Kumar, S. M. Girvin and R. J. Schoelkopf, Strong coupling of a single photon to a superconducting qubit using circuit quantum electrodynamics, Nature **431**, 162 (2004).

[9] M. H. Devoret, S. M. Girvin and R. J Schoelkopf, Circuit-QED: How strong can the coupling between a Josephson junction atom and a transmission line resonator be?, Annalen der Physik, **16**, 767 (2007).

[10] F. Yoshihara, T. Fuse, Z. Ao, S. Ashhab, K. Kakuyanagi, S. Saito, T. Aoki, K. Koshino, and K. Semba, Circuit quantum electrodynamics in the ultrastrong-coupling regime., Phys. Rev. Lett. **120**, 183601 (2018).

[11] F. Yoshihara, T. Fuse, S. Ashhab, K. Kakuyanagi, S. Saito and K. Semba, Superconducting qubit–oscillator circuit beyond the ultrastrong-coupling regime, Nature Phys. B **13**, 44 (2017).

[12] T. Niemczyk, F. Deppe, H. Huebl, E. P. Menzel, F. Hocke, M. J. Schwarz, J. J. Garcia-Ripoll, D. Zueco, T. Hümmer, E. Solano, A. Marx and R. Gross, Circuit quantum electrodynamics in the ultrastrong-coupling regime, Nature Phys. B **6**, 772–776 (2010).

[13] A. Baust, E. Hoffmann, M. Haeberlein, M. J. Schwarz, P. Eder, J. Goetz, F. Wulschner, E. Xie, L. Zhong, F. Quijandría, D. Zueco, J. J. García Ripoll, L. García-Álvarez, G. Romero, E. Solano, K. G. Fedorov, E. P. Menzel, F. Deppe, A. Marx and R. Gross, Ultrastrong coupling in two-resonator circuit QED, Phys. Rev. B **93**, 214501 (2016).

[14] P. Forn-Díaz, L. Lamata, E. Rico, J. Kono, E. Solano, Ultrastrong coupling regimes of light-matter interaction, Rev. Mod. Phys. **91**, 025005 (2019).

[15] P. Forn-Díaz, J. J García Ripoll, B. Peropadre, J.-L. Orgiazzi, M. A. Yurtalan, R. Belyansky, C. M. Wilson, A. Lupascu, Ultrastrong coupling of a single artificial atom to an electromagnetic continuum in the nonperturbative regime, Nature Phys **13**, 39 (2017).

[16] J. Bourassa, J. M. Gambetta, A. A. Abdumalikov, Jr., O. Astafiev, Y. Nakamura, and A. Blais, Ultrastrong coupling regime of cavity QED with phase-biased flux qubits, Phys. Rev. A **80**, 032109 (2009).

[17] A. Zagoskin and A. Blais, Superconducting qubits, arXiv:0805.0164 [Condensed Matter, V **63** 215 (2008)].

[18] S. Dominik and S. Kais, Magnetic flux noise in superconducting qubits and the gap states continuum, Sci Rep. B **11**, 1813 (2021).

[19] W. D. Oliver and P. B. Welander, Materials in superconducting quantum bits. MRS Bulletin B **38**, 816 (2013).

[20] R. H. Koch, D. P. DiVincenzo, and J. Clarke, Model for 1/f Flux Noise in SQUIDs and Qubits, Phys. Rev. Lett. **98**, 267003 (2007).

[21] L. Faoro and L. B. loffe, Microscopic origin of low-frequency flux noise in Josephson circuits, Phys. Rev. Lett. **100**, 227005 (2007).

[22] S. Choi, D. H Lee, S. G. Louie and J. Clarke, Localization of metal-induced gap states at the metal–insulator interface: origin of flux noise in squids and superconducting qubits, Phys. Rev. Lett. **103**, 197001 (2009).

[23] O. Jessensky, F. Müller and U. Gösele, Self-organized formation of hexagonal pore arrays in anodic alumina, Appl. Phys. Lett. A**72**, 1173 (1998).

[24] D. Bothner, C. Clauss, E. Koroknay, M. Kemmler, T. Gaber, M. Jetter, M. Scheffler, P. Michler, M. Dressel, D. Koelle, and R. Kleiner, Reducing vortex losses in superconducting microwave resonators with microsphere patterned antidot arrays, Appl. Phys. Lett. **100**, 012601 (2012).

[25] D. Bothner, T. Gaber, M. Kemmler, D. Koelle, and R. Kleiner, Improving the performance of superconducting microwave resonators in magnetic fields, Appl. Phys. Lett. A**98**, 102504 (2011).

[26] C. Song, M. P. DeFeo, K. Yu, and B.L.T. Plourdea, Reducing microwave loss in superconducting resonators due to trapped vortices, Appl. Phys. Lett. **95**, 232501 (2009).

[27] U. Welp, Z.L. Xiao, J.S. Jiang, V.K. Vlasko-Vlasov, S.D. Bader, G.W. Crabtree, J. Liang, H. Chik, and J.M. Xu, Superconducting transition and vortex pinning in Nb films patterned with nanoscale hole arrays, Phys. Rev. B **66**, 212507 (2002).

[28] A. Ronzani, B. Karimi, J. Senior, Y.-C. Chang, J.T. Peltonen, C. Chen and J.P. Pekola, Tunable photonic heat

transport in a quantum heat valve, Nat. Phys. **14**, 991 (2018).

[29] J. Senior, A. Gubaydullin, B. Karimi, J. T. Peltonen, J. Ankerhold, and J. P. Pekola, Heat rectification via a superconducting artificial atom, Commun Phys **3**, 40 (2020).

[30] G. J Dolan, Offset masks for lift-off photoprocessing, Appl. Phys. Lett. **31**, 337 (1977).

[31] M.S. Khalil, M.J.A. Stoutimore, F.C. Wellstood and K.D. Osborn1, An analysis method for asymmetric resonator transmission applied to superconducting devices, J. Appl. Phys. **111**, 054510 (2012).

[32] C. Deng, M. Otto and A. Lupascu, An analysis method for asymmetric resonator transmission applied to superconducting devices, J. Appl. Phys. **114**, 054504 (2013).

[33] S. Probst, F. B. Song, P. A. Bushev, A. V. Ustinov and M. Weides, Efficient and robust analysis of complex scattering data under noise in microwave resonators, Review of Scientific Instruments **86**, 024706 (2015).

[34] Y.-C. Chang, B. Karimi, J. Senior, A. Ronzani, J. T. Peltonen, H.-S. Goan, C.-D. Chen, and J. P. Pekola, Utilization of the superconducting transition for characterizing low-quality-factor superconducting resonators, Appl. Phys. Lett. 115, 022601 (2019).

[35] M. Göppl, A. Fragner, M. Baur, R. Bianchetti, S. Filipp, J. M. Fink, P. J. Leek, G. Puebla, L. Steffen, A. Wallraff, Coplanar Waveguide Resonators for Circuit Quantum Electrodynamics, J. Appl. Phys. **104**, 113904 (2008).

[36] D. M. Pozar, Microwave Engineering, 4th ed. Wiley, Hoboken, NJ, (2012).

[37] B. Karimi and J.P. Pekola, Otto refrigerator based on a superconducting qubit: Classical and quantum performance, Phys. Rev. B **94**, 184503 (2016).